Progress Towards Fuselage Drag Reduction via Active Flow Control: A Combined CFD and Experimental Effort

Norman W. Schaeffler[*], **Brian G. Allan**[†]
NASA Langley Research Center, Hampton, Virginia, USA

Caroline Lienard[‡], **Arnaud Le Pape**[§]
ONERA, Meudon, France

Abstract

A combined computational and experimental effort has been undertaken to study fuselage drag reduction on a generic, non-proprietary rotorcraft fuselage by the application of active flow control. Fuselage drag reduction is an area of research interest to both the United States and France and this area is being worked collaboratively as a task under the United States/France Memorandum of Agreement on Helicopter Aeromechanics. In the first half of this task, emphasis is placed on the US generic fuselage, the ROBIN-mod7, with the experimental work being conducted on the US side and complementary US and French CFD analysis of the baseline and controlled cases. Fuselage simulations were made using Reynolds-averaged Navier-Stokes flow solvers and with multiple turbulence models. Comparisons were made to experimental data for numerical simulations of the isolated fuselage and for the fuselage as installed in the tunnel, which includes modeling of the tunnel contraction, walls, and support fairing. The numerical simulations show that comparisons to the experimental data are in good agreement when the tunnel and model support are included. The isolated fuselage simulations compare well to each other, however, there is a positive shift in the centerline pressure when compared to the experiment. The computed flow separation locations on the rear ramp region had only slight differences with and without the tunnel walls and model support. For the simulations, the flow control slots were placed at several locations around the flow separation lines as a series of eight slots that formed a nearly continuous U-shape. Results from the numerical simulations resulted in an estimated 35% fuselage drag reduction from a steady blowing flow control configuration and a 26% drag reduction for unsteady zero-net-mass flow control configuration. Simulations with steady blowing show a delayed flow separation at the rear ramp of the fuselage that increases the surface pressure acting on the ramp, thus decreasing the overall fuselage pressure drag.

[*]n.w.schaeffler@nasa.gov
[†]brian.g.allan@nasa.gov
[‡]caroline.lienard@onera.fr
[§]Arnaud.Lepape@onera.fr

Nomenclature

x/R	=	Normalized streamwise coordinate
y/R	=	Normalized cross-stream coordinate
z/R	=	Normalized vertical coordinate
R	=	Reference rotor radius
f	=	Excitation frequency, Hz
W	=	Fuselage width (maximum)
H	=	Fuselage height (maximum)
A_{CS}	=	Fuselage cross-sectional area (maximum)
P	=	Pressure
P_s	=	Static pressure
q	=	Freestream dynamic pressure $\equiv 1/2\rho_\infty U_\infty^2$
Re	=	Reynolds number based on fuselage length, $\equiv U_\infty(2R)/\nu$
M	=	Mach number $\equiv U_\infty/a_\infty$
C_D	=	Drag coefficient $\equiv Drag/(qA_{CS})$
C_L	=	Lift coefficient $\equiv Lift/(qA_{CS})$
C_p	=	Pressure coefficient $\equiv (P-P_s)/q$
F^+	=	Reduced frequency $\equiv fW/U_\infty$
C_μ	=	Momentum coefficient, $\equiv \sum(\rho_j A_j U_j^2)/(qA_{CS})$
U_∞	=	Freestream velocity
U_j	=	Jet exit peak velocity
A_j	=	Jet slot area
α_j	=	Jet inclination angle, degrees
ϕ	=	Jet phase angle, degrees
α	=	Angle of attack, degrees
a_∞	=	Freestream speed of sound
ν	=	Kinematic viscosity
ρ	=	Density

1 Introduction

The design of a rotorcraft fuselage is driven more by the future function of the vehicle than by its aerodynamic efficiency. This makes the rotorcraft fuselage more closely related aerodynamically to a ground utility vehicle than to a fixed-wing aircraft. As such, it has been noted that the cruise drag of a rotary-wing aircraft is an order of magnitude higher than the cruise drag of a fixed-wing aircraft of the same gross weight [1] and that, at high advance ratio, half of the power delivered by the main rotor is used to overcome the aerodynamic forces acting on the fuselage [2]. The bluff-body characteristics of the flowfield around a rotorcraft fuselage is typically domi-

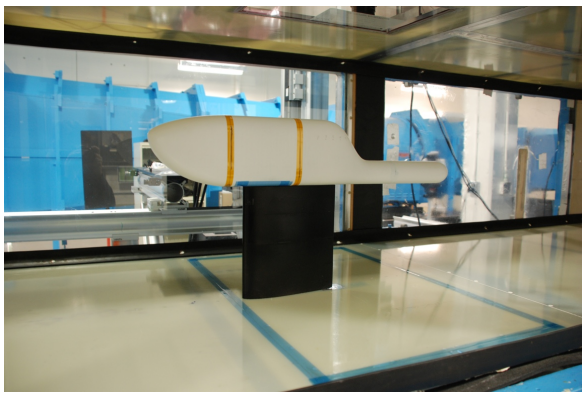

(a) Model is installed in the tunnel in an inverted configuration.

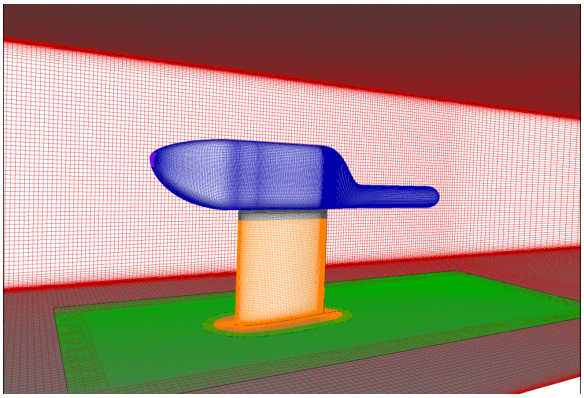

(b) Mesh for baseline CFD simulation with tunnel walls and model support.

Figure 1: Experimental and Computational setup of the ROBIN-mod7 model as installed in the 2x3 BLC Tunnel.

nated by a massive flow separation around the aft end of the fuselage. This results not only in a large amount of pressure drag, but also in a wake that tends to become unsteady, which can introduce unsteady loads to the tail boom, stabilizers and tail rotor. The work of Martin, et. al. [3] and Ben-Hamou et. al. [4] has demonstrated that the application of active flow control to achieve a reduction in fuselage drag is possible. In order to better understand the mechanisms by which a reduction in fuselage drag is achievable, the underling flow physics for both the uncontrolled baseline and the controlled case must be understood in as much detail as possible. To gain this insight, an effort was undertaken to study fuselage drag reduction on a generic fuselage by the NASA Subsonic Rotary Wing (SRW) Project as an integrated experimental and CFD effort. It is a major goal of the SRW Project to advance the state-of-the-art in modeling all aspects of rotorcraft aeromechanics.

Given that fuselage drag reduction is an area of research interest to both France and the United States, this area is being worked collaboratively as a task under the United States/France Memorandum of Agreement (MOA) on Helicopter Aeromechanics. The research efforts for this task are being conducted by NASA, on the US side, and ONERA, on the French side. Each side is independently conducting an experimental effort on their own fuselage design, with both sides performing computations on both fuselages. The present paper details elements of the NASA fuselage drag reduction experiment and the complementary NASA and ONERA CFD analysis of the baseline and controlled flowfields. The experiment and the detailed computations will provide the necessary insight into the flow physics involved in the baseline flowfield and in its control. The need for a non-proprietary fuselage was identified early on. An open, non-proprietary fuselage would permit the widest possible dissemination of the fuselage geometry and its aerodynamic characteristics. With these goals in mind, a modified version of the ROBIN (ROtor Body INteraction) fuselage was selected as the basis for the US research effort. The ROBIN fuselage was developed at NASA Langley in the 1970s to be representative of a generic helicopter and also to be easily reproduced for calculations [5]. It has been utilized in several other wind tunnel investigations [6, 7] and is widely used in the rotorcraft CFD community [8, 9]. The standard coefficients that define the ROBIN fuselage shape were modified to create a new fuselage shape that has a rectangular, as opposed to square cross-section, a well-defined ramp section and a high tail boom. This modified version of the ROBIN fuselage will be referred to as the ROBIN-mod7. The fuselage calculation procedure and the modified coefficients for the ROBIN-mod7 are discussed fully in Appendix A. It is hoped that the ROBIN-mod7 fuselage can be established as a standard test fuselage for evaluating different AFC strategies both experimentally and computationally.

2 Experimental Facility, Model, and Instrumentation

The experimental testing of the ROBIN-mod7 was conducted in the 2-Foot x 3-Foot Boundary Layer Channel (2 x 3) Wind Tunnel, located at NASA Langley Research Center. The wind tunnel is a closed-circuit tunnel which features a 10:1 contraction ratio and a test section that is 24 inches (0.61 m) high, 36 inches (0.91 m) wide and 20 feet (6.1 m) long. The maximum speed for the tunnel is approximately 45 m/s. Within the test section, the freestream turbulence intensities are approximately 0.1% within a frequency range of $0.1 < f < 400$ Hz. Both the floor and the ceiling of the tunnel feature adjustable support points that make it possible to tailor the pressure gradient down the tunnel in the streamwise direction. For the current research effort, the floor and ceiling were set to be level. This results in a pressure gradient down the tunnel that was documented with empty tunnel runs before the model installation. Additional information about the facility can be found in King and Breuer [10]. A view of the model installed in the test section of the 2 x 3 Wind Tunnel test section can be

seen in Figure 1(a). The model is installed in the 2 x 3 Wind Tunnel in an inverted position.

The ROBIN-mod7 fuselage model is 28.235 inches (0.7172 m) in length and was tested as an isolated fuselage. Based on the scaling of the ROBIN fuselage, the model length is the same as the diameter of a representative rotor that would be paired with the fuselage. In other words, the model length is 2R, where R is the representative rotor radius that will serve as the characteristic length for normalization of the fuselage coordinates. Therefore, for the 2x3 model, the reference "rotor" radius, R, is 14.1177 in (0.3586 m). The model is constructed around an aluminum central spine, which has an aluminum bulkhead at each end. The spine and bulkheads are internal to the model with the nose of the fuselage being attached to the forward bulkhead and the tail and tail boom attached to the aft bulkhead. In between the two bulkheads is the constant cross-section body of the fuselage.

It is in the body section that the vertical post which supports the model is attached to the central spine. The post is located at a fuselage station, $x/R = 0.690$, which would correspond to the rotor shaft location. The other end of the post is mounted, externally to the tunnel, to a force balance that allows the drag force acting on the model to be measured directly. The post is isolated from the flow in the tunnel by a fairing, utilizing a NACA 0018 profile, that is mounted to the floor of the tunnel. For each of the two angles of attack considered, 0° and −5°, there is a custom fairing which maintains a uniform air gap, 0.10 inches, between the top of the fairing and the bottom of the model. The force balance consists of an air bearing slide that restrains motion in all directions except in the streamwise direction along the centerline of the tunnel test section. Motion in the streamwise direction is restrained by a load cell with a 1.1 pound (4.89 N) range. The output from the load cell is amplified and filtered by a signal conditioner before being digitally sampled by a high-speed 16-bit Analog-to-Digital convertor.

The baseline model is instrumented with a total of 41 static pressure taps. These static pressure taps are connected to an electronically scanned pressure transducer mounted inside the model atop the central spine to keep the tubing runs as short as possible. Additionally, there are 32 static pressure taps on the floor and 15 static pressure taps on the ceiling. The model coordinate system was adopted for the locations of the floor and ceiling pressure taps, i.e., the nose of the fuselage is located at $x/R = 0.00$, the support post is located at $x/R = 0.690$ and the end of the tailboom is located at $x/R = 2.00$. Therefore, the floor taps on the centerline of the test section extend from $x/R = -3.340$, which is upstream of the model, to $x/R = 1.689$. The floor taps closest to the model, those located at stations greater than $x/R = 0.361$, are shifted off the centerline to a position halfway between the centerline and the wall, $y/R = -0.637$, because of the fairing. The ceiling taps are located on the centerline of the tunnel and start at $x/R = 2.291$ and extend downstream to $x/R = 8.241$. The floor and ceiling pressure taps are each instrumented with their own electronically scanned pressure transducers. All of the pressure measurements are referenced to the tunnel static pressure, as measured by a Pitot-static probe located upstream of the model at $x/R = -2.950$. The primary condition for the data acquisition was a freestream velocity of approximately 34 m/s, corresponding to a Mach number of 0.10 and a Reynolds number, based on the length of the fuselage, of 1,600,000.

3 Numerical Approach

3.1 OVERFLOW Flow Solver (NASA)

The flow field for the fuselage was computed using the flow solver code, OVERFLOW [11, 12] developed at NASA. This code solves the compressible RANS equations using the diagonal scheme of Pulliam and Chaussee [13]. The RANS equations are solved on structured grids using the overset grid framework of Steger, Dougherty, and Benek [14]. The flow is computed on node-centered grids composed of curvilinear body-fitted grids overset onto automatically generated Cartesian block background grids. Convergence and accuracy of the flow solution was improved using a Low-Mach number Preconditioning (LMP) option for steady simulations. The numerical simulations were performed using the parallel version of the OVERFLOW code developed by Buning [15]. This code uses the Message-Passing Interface (MPI) and can run on a tightly-coupled parallel machine or a network of workstations. The code distributes zones to individual processors and can split larger individual zones across multiple processors using a domain decomposition approach.

The RANS equations are solved implicitly using the Beam-Warming block tridiagonal scheme with a 3^{nd} order Roe upwind scheme for the inviscid flux terms. The Shear Stress Transport (SST) and Spalart Allmaras (SA) turbulence models were both used for the numerical simulations and compared to experimental results [16, 17]. A Rotational/Curvature Correction (RCC) model, as implemented in OVERFLOW, was evaluated for both turbulence models [18].

The blowing jets in OVERFLOW were simulated using a surface boundary condition, simplifying placement of the jets on the fuselage. The jet properties were defined by setting a mass flow ratio per unit area of, $\rho_j U_j / \rho_\infty U_\infty$ and the total temperature ratio, $T_{tj}/T_{t\infty}$. For slots, a jet blowing angle, α_j, can also be specified and is based on the local surface tangent, normal to the slot span. An α_j of 90° is therefore normal to the local surface and 0° is tangent to the local surface and normal to the slot local spanwise tangent.

Since the blowing slots intersect the fuselage surface at an angle α_j, the width of the jet boundary condition on the surface is given by:

$$w = h / \sin(\alpha_j) \tag{1}$$

where w is the width of the slot on the surface and h is the flow control slot height.

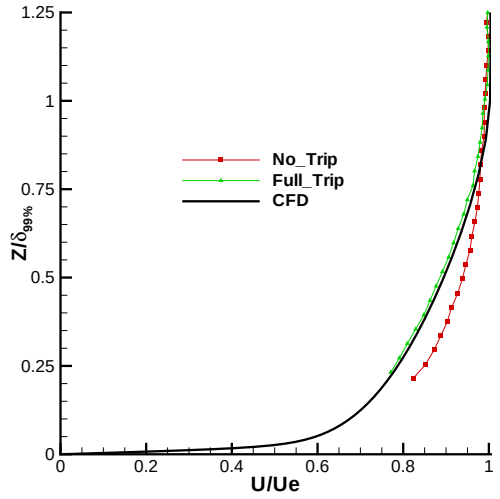

Figure 2: Comparison of the centerline boundary layer profiles at x/R=0.900 from the experiment and the OVERFLOW simulation for 0° angle of attack for a free stream Mach number of 0.1.

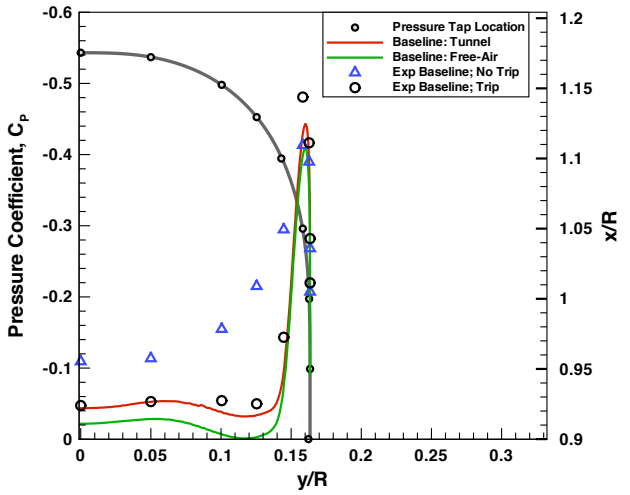

Figure 3: Spanwise C_P profile at $z/R = -0.075$ for the experiment for the untripped and the fully tripped case. The OVERFLOW baseline results are for simulation with the tunnel wall and for free-air.

3.2 elsA Flow Solver (ONERA)

The elsA (French acronym for "Ensemble Logiciel de Simulation en Aérodynamique") software [19] is dedicated to the numerical simulation of the compressible viscous mono-species, steady and unsteady fluid flows, on three dimensional (or two-dimensional, or axisymmetric) multi-block structured meshes. It solves the compressible RANS equations in a finite volume cell-centered formulation. Overlapping grid treatment capability is also available in elsA allowing the same grid to be utilized by both OVERFLOW and elsA. In the present paper, most cases are computed using a 2nd-order Jameson scheme with the addition of numerical dissipation. The time integration is performed by a LUSSOR algorithm combined with a backward Euler scheme. A low-Mach preconditioning method is used to enhance convergence and accuracy. In the case of unsteady computations, a Newton method based on the Gear algorithm is used. Various turbulence models are implemented in elsA, but the k-ω Kok model was mainly used for the fully-turbulent simulations from ONERA.

The blowing jets in elsA were also simulated using a surface boundary condition. The properties for steady jets were derived from a direction, the desired local flow per unit of area, and the desired stagnation enthalpy. In the case of unsteady blowing, the jet is specified by a direction, an average velocity, velocity amplitude, frequency and phase. The blowing boundary conditions in elsA were designed for jets with internal cavities where the surface to which the boundary condition is applied is planar and the incoming flow has a single orientation relative to the normal of that planar boundary.

Adapting this planar surface boundary condition to a slot on the surface of the fuselage that has curvature introduces some complications. The flow from each slot is required to have a uniform direction, defined in the global reference frame. This uniform direction is determined by calculating the average local surface tangent along the slot and then adding the desired jet angle. The velocity magnitude along the slot is also affected by the slot curvature. Any degree of curvature will result in a non-uniform velocity profile at the slot. For slots with a large change in curvature from end to end, this non-uniformity can be significant.

Due to the differences between the implementation of the blowing boundary condition in OVERFLOW and elsA, the results for the flow control cases are not quantitatively compared in this paper.

4 Results and Discussions

Since this is the first time that the aerodynamic characteristics of the ROBIN-mod7 have been studied, documentation of its baseline aerodynamics was required. Experimentally, the foundation for this documentation is the surface pressure distribution and the measurement of the drag force and these data will be presented in comparison to the corresponding computational values.

The exact location from where the flow separates from the model will determine the measured or computed drag value, so identifying these locations is important when it comes time to make comparisons between the experimental values and the computed values. The state of the boundary layer, especially upstream of the separation line before the ramp, was a point of concern when comparing the experimental data to the computational data. To insure a fully-developed turbulent boundary layer, a boundary layer trip was required near the nose of the model. The complete trip was built up and documented a section at a time starting with a trip in the spanwise direction near the nose on the lower fuselage surface. The location of the trip relative to the stagnation point, located on the upper surface, was selected using the method of Braslow and Knox [20]. The trip was then extended up the side of the model. A trip was

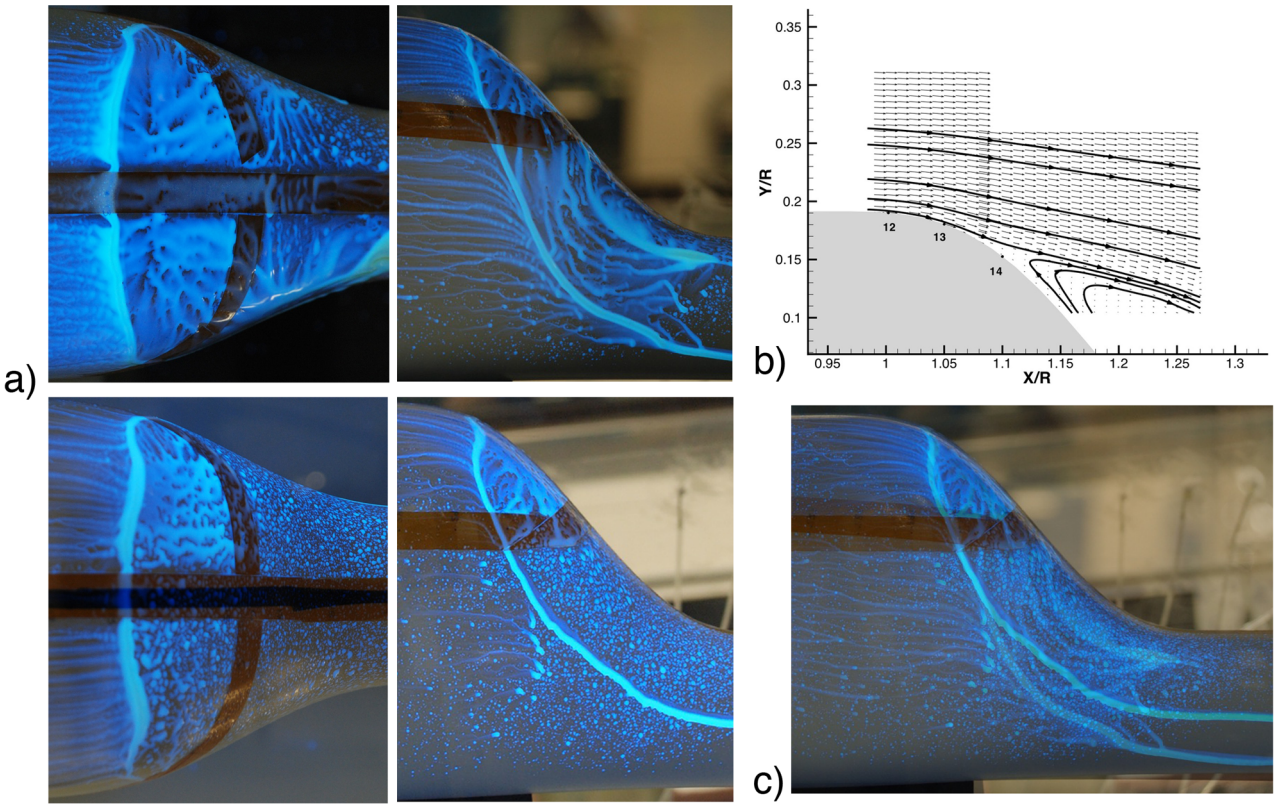

Figure 4: UV Oil flow visualization and PIV measurements of the baseline separation location. a)UV Oil Flow Visualization for $\alpha = 0°$ (Top Row) and for $\alpha = -5°$ (Bottom Row), (b)Velocity field for $\alpha = 0°$, (c)Overlay of two side views

also placed on the upper fuselage surface using the same distance from the stagnation location as the for the lower trip. The effectiveness of the trip was documented using the centerline PIV data. In Figure 2, the velocity profile extracted just upstream of the start of the ramp, at x/R = 0.900, from the centerline PIV data is presented for the tripped and un-tripped condition along with the corresponding velocity profile at that location from the computation. It can be seen that the tripped boundary layer profile matches the CFD profile closer than the un-tripped profile. The truncation of the PIV-measured profile close to the wall is due to surface glare off the model affecting the measurement. Physically, this affected region is on the order of 1 mm off the surface. Installing the trip has a similar effect on the comparison of the spanwise surface pressure distribution. There is a line of surface pressure taps in the spanwise direction, halfway down the ramp at $z/R = -0.075$. The data at this location, which is presented in Figure 3, shows a better agreement for the tripped condition than the un-tripped condition. Once the trip was set, the model remained tripped for the rest of the experiment.

The separation locations for the cases considered were documented in the experiment by the use of surface pressure measurements, surface oil flow visualization, and particle image velocimetry (PIV). The separation location can be most clearly seen in the surface oil flow visualization, where portions of the model are sprayed with a mixture of alcohol and aircraft motor oil, which contains a fluorescent additive [21]. Once the oil flow pattern is stable and photographed under ultraviolet lights, the resulting patterns, which can be seen in Figure 4, indicate that flow separates in a continuous U-shaped line which is symmetric around the centerline. On the centerline upstream of the ramp, the flow separates slightly upstream of the static pressure tap located at an x/R = 1.050. For the 0° case, this location is verified by the PIV measurements taken as shown in Figure 4b. Along the side of the model, the separation line is inclined to the streamwise direction and crosses the z/R=-0.075 line of pressure taps near the tap located at y/R=0.1447. The surface oil flow visualizations done for the −5° case indicate that the location of the separation line does not shift significantly with the change in angle of attack (Figure 4a). This is a encouraging finding for the application of flow control.

Additionally, the sensitivity of the drag coefficient, C_D, of the ROBIN-mod7 to changes in the Mach number was documented. For the 0° angle of attack case, the C_D was found to be approximately constant above a Mach number of 0.090. For the −5° angle of attack case, the C_D shows even less sensitivity to Mach number as it does for the 0° angle of attack case, effectively being constant over the observed range from 0.07 to 0.100.

4.1 Baseline

4.1.1 0° Angle of Attack

Baseline numerical simulations were performed matching the experiment for the model at 0° angle of attack.

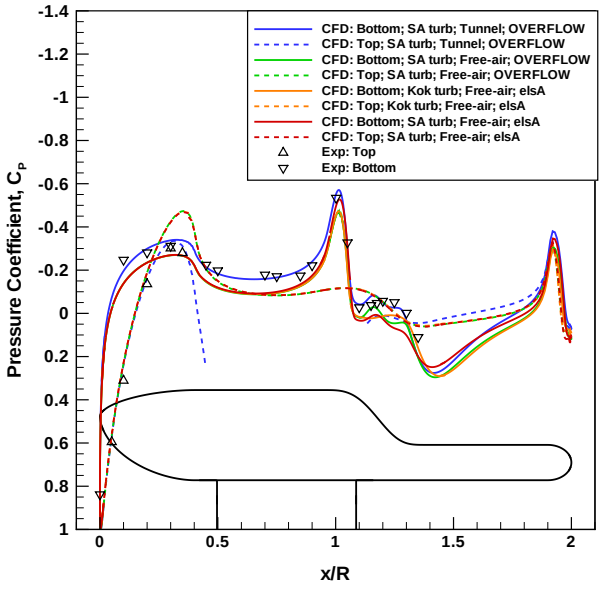

Figure 5: Comparison of the centerline surface C_P values from the baseline CFD simulations and the experiment for 0° angle of attack for a free stream Mach number of 0.1

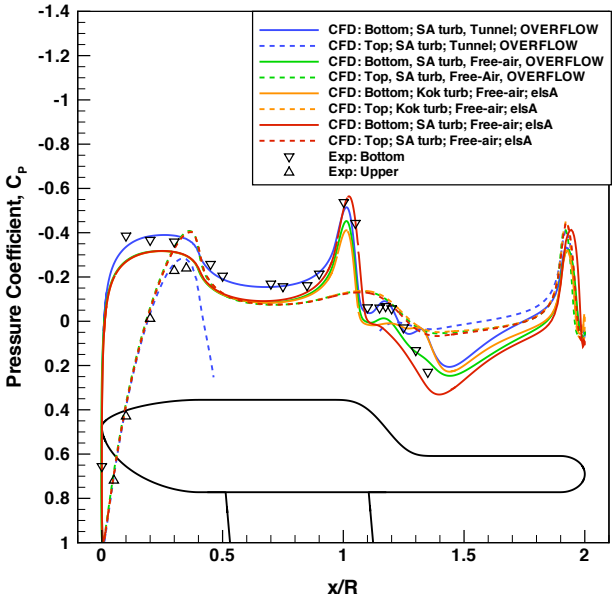

Figure 6: Comparison of the centerline surface C_P values from the baseline CFD simulations and the experiment for - 5° angle of attack for a free stream Mach number of 0.1.

Figure 1(b) shows the baseline fuselage grid with the tunnel and model support. The main fuselage grid had 251 grid points in the circumferential direction and 477 points along the fuselage with 61 points normal to the surface. The body grid was composed of a main fuselage with cap grids on the nose and tail and had a total of 7.8 million grid points. The tunnel simulation with the body and tunnel grids had a total of 35 million grid points.

The baseline centerline C_P values are compared to the experimental data in Figure 5. This comparison shows that the CFD matches the experimental data well when modeling the tunnel walls and models support. The free-air simulations using SA (OVERFLOW, elsA) and k-ω Kok (elsA) turbulence models compare well to each other, however, there is a positive shift in the centerline pressure when compared to the experiment. The pressure coefficients obtained using k-ω Kok (elsA) are slightly different from other numerical results but seem to capture the separation length well.

A summary of C_D values is given in Table 1 for the experiment and CFD at 0° angle of attack. This table shows the contribution to the overall fuselage drag coefficient and a break down of the viscous and pressure contributions. A comparison of the OVERFLOW results using the SST and SA models for the 0° case with tunnel walls shows a similar viscous contribution to the drag with the SST model having a higher pressure drag component. The higher pressure drag from the OVERFLOW SST simulation is a result of an earlier flow separation than either of the other two models. This early separation by the SST model results in a lower base pressure and thus larger pressure drag as compared to the other models. A comparison of total C_D for the 0° case shows that the OVERFLOW simulation with tunnel walls and the SA model is the closest to matching the measured drag from the experiment.

A comparison was made using OVERFLOW with the SA turbulence model using the same body grid in both free-air and with the wind tunnel wall and model support. This comparison of the OVERFLOW simulations shows that the free-air results have a 28% lower drag as compared to the simulation with the tunnel walls. Table 1 shows that the main difference between these two cases is a large reduction of the pressure drag contribution for the free-air case. The elsA free-air simulations using the SST and k-ω Kok turbulence models predict a lower viscous drag contribution as compared to the OVERFLOW SA and SST free-air results with the elsA SA model showing a slightly higher viscous drag component as compared to OVERFLOW with the SA model. The elsA free-air results for the SA and k-ω Kok models are predicting a lower pressure drag component as compared to the OVERFLOW free-air SA and is indicative of a delayed separation. The elsA free-air simulation using the SST model has a pressure drag contribution of 0.061 and is similar to the OVERFLOW free-air SA value of 0.058.

Therefore in order to match the experimental drag and pressures, simulations must include the tunnel tunnel walls and model support. Despite these differences in simulations with and without the tunnel walls and model support, the flow separation locations on the rear ramp region had only slight differences. Since the separation location is not sensitive to the tunnel walls and model support, the free-air simulations can then be used for the development and evaluation of the flow control for fuselage drag reduction.

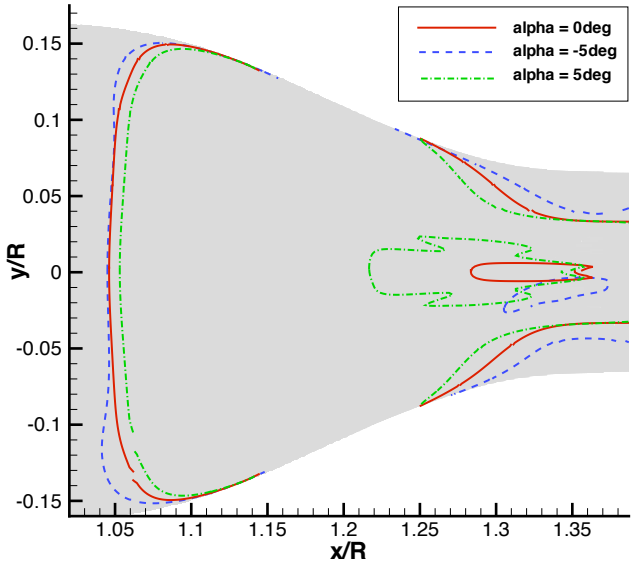

(a) Bottom View

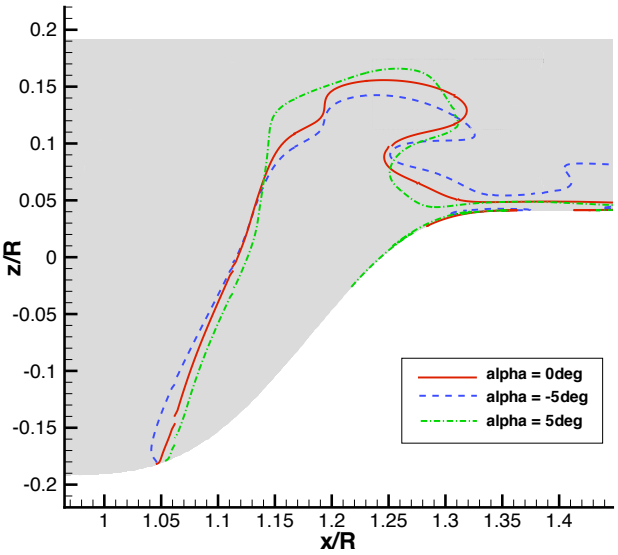

(b) Side View

Figure 7: Baseline separation location from CFD simulations for $\alpha = 0°$, $\alpha = -5°$, and $\alpha = 5°$ for a free stream Mach number of 0.100 (a) bottom view and (b) side view, (elsA results)

0° Angle of Attack Case

			C_{Dvisc}	C_{Dpress}	C_D
OVERFLOW	SST	tunnel	0.058	0.111	0.169
OVERFLOW	SA	tunnel	0.055	0.090	0.145
OVERFLOW	SA	free-air	0.056	0.058	0.114
elsA	KOK	free-air	0.051	0.050	0.101
elsA	SST	free-air	0.051	0.061	0.112
elsA	SA	free-air	0.059	0.050	0.109
EXP					0.145

Table 1: Summary of the baseline drag comparison between CFD and experiment for the fuselage at 0° angle of attack. CFD drag is broken down into viscous and pressure contributions on the fuselage for both the tunnel and free-air simulations.

-5° Angle of Attack Case

			C_{Dvisc}	C_{Dpress}	C_D
OVERFLOW	SST	tunnel	0.057	0.112	0.169
OVERFLOW	SA	tunnel	0.057	0.091	0.148
OVERFLOW	SA	free-air	0.056	0.066	0.122
elsA	KOK	free-air	0.052	0.053	0.105
elsA	SA	free-air	0.060	0.058	0.118
EXP					0.153

Table 2: Summary of the baseline drag comparison between CFD and experiment for the fuselage at -5° angle of attack. CFD drag is broken down into viscous and pressure contributions on the fuselage for both the tunnel and free-air simulations.

4.1.2 -5° Angle of Attack

A comparison of total C_D for the -5° case is given in Table 2. This table shows the OVERFLOW SA model with the tunnel walls to be 3% lower than the balance drag from the experiment. Like the 0° case, the total C_D for the OVERFLOW SA free-air simulation in Table 2 results in a 18% lower drag as compared to the OVERFLOW SA full-tunnel simulation, with the main difference seen in the pressure drag. As in the 0° case, the elsA free-air results predict a lower total drag as compared to OVERFLOW with the elsA k-ω Kok model predicting a 14% lower drag than the OVERFLOW SA model free-air results. The main difference between the elsA and OVERFLOW free-air results for the -5° case is in the pressure drag component indicating that the free-air OVERFLOW results are predicting an earlier separation as compared to elsA simulations using the k-ω Kok and SA models.

The pressure distribution for the model at -5° angle of attack is shown in Figure 6 for OVERFLOW with the SA model, for elsA with the SA and k-ω Kok models and for the experiment. Overall the CFD results with the tunnel modeled compare well to the experiment, however there is a significant difference in the surface pressures at the end of the ramp near the tail boom. The free-air pressure for the -5° case has a similar pressure offset compared to the experimental data as was seen in the 0° case due to the effects of the tunnel walls and model support. The differences between SA and k-ω Kok models from elsA are more significant for the -5° case than for the 0° case, with respect to both the pressure coefficient and the drag values. Moreover, the numerical results combined with oil flow visualization tend to confirm that the separation line position does not change significantly with angle of attack from 0° to -5° (Figure 4 and 7).

4.2 Grid Resolution Study

A grid resolution study was made for the baseline free-air case at 0° and -5° angle of attack. Table 3 summarized the grid resolution for the three levels of grids.

Grid	Main Body	Body Points	Total Points
coarse	169×101×41	778,631	10,455,503
medium	337×201×81	6,089,499	25,554,482
fine	673×401×161	48,163,955	87,918,147

Table 3: Summary of the mesh sizes for a grid resolution study. Body grids consist of a main body grid, nose cap, and tail cap grid. The total points for the 3 body grids is given in the body points column and the total number of points for the body and background grids is given in the total points column.

Grid	C_D $\alpha = 0°$	$\%C_D$ $\alpha = 0°$	C_D α =-5°	$\%C_D$ α =-5°
coarse	0.1150	0.61	0.1265	7.02
medium	0.1147	0.40	0.1226	3.72
fine	0.1144	0.10	0.1193	0.93
RE m-c	0.1146	0.33	0.1213	2.62
RE f-m	0.1143	–	0.1213	–

Table 4: Summary of the baseline drag results for a grid resolution study using OVERFLOW with the SA turbulence model. The percentage differences are from changes from the "RE f-m" results.

The medium grids were made by removing every other point in the fine grid and the coarse grids by removing every other point in the medium grids. Note that the medium grid is representative of the resolution used for the simulations with tunnel walls and model support. The results from this study are given in Table 4 for both the 0° and -5° angle of attack cases. This table also shows the Richardson Extrapolation (RE) results using the medium and coarse grids (RE m-c) and using the fine and medium grids (RE f-m). The percentage difference from the RE using the fine and medium grids has also been computed. This percentage difference shows that there is little difference for the 0° case with the medium grid having a 0.40% difference. The -5° case shows a larger percentage difference with the medium grid having a 3.7% difference. The -5° case did not asymptotically converge like the 0° case as a result of some unsteadiness in the steady-state flow calculations. Overall, both cases are showing good grid resolution convergence for the baseline calculations.

4.3 Flow Control CFD

Results from the numerical simulations of steady and unsteady flow control and its effect on fuselage drag will now be discussed. In this investigation, the CFD was used to develop a flow control strategy and identify actuator design parameters needed for the experiment. There are many different flow control approaches such as, blowing slots, steady jets, sweeping jets, and zero-mass-flux (synthetic) jets, as well as passive devices such as vortex generating vanes. The focus of this study is to evaluate steady blowing and Zero-Net-Mass-Flux (ZNMF) blowing in order to better understand the effects of the slots on the fuselage drag. A better understanding of the flow

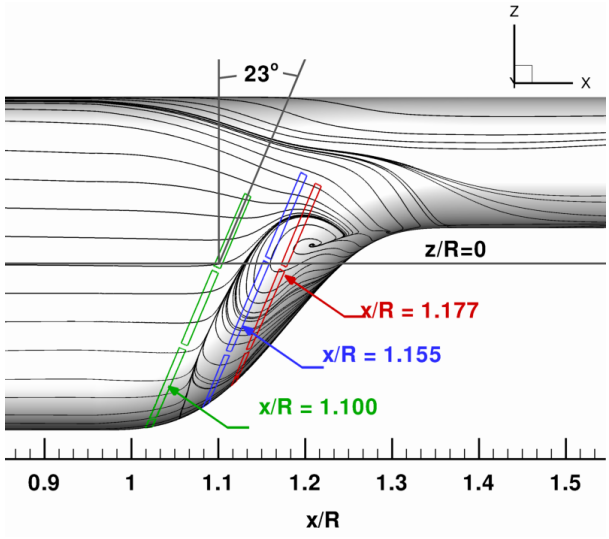

Figure 8: Side view of slot locations and surface streamlines from the baseline flow calculations.

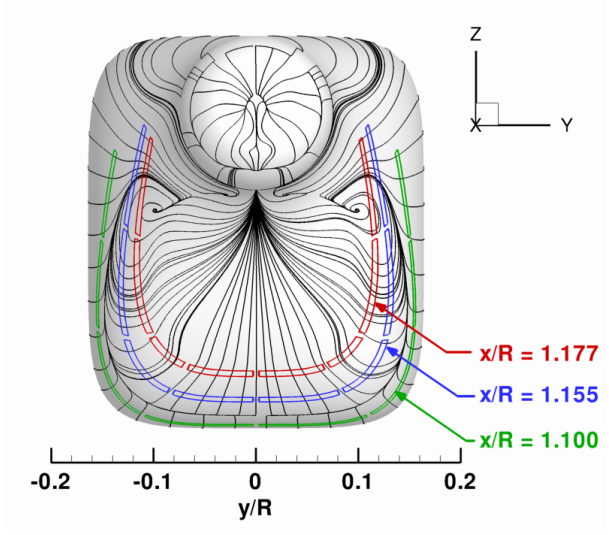

Figure 9: Rear view of slot locations, illustrating the U-shaped pattern of the slots, and the surface streamlines from the baseline flow calculations.

mechanism that will reduce the drag will help provide guidance on future flow control approaches that may improve the overall system performance.

4.3.1 Flow Control Slots

The same slot locations were used for both steady blowing and zero-net-mass blowing. These flow control slots were placed near the flow separation region with a jet inclination angle of α_j. Three similarly constructed slot arrangements were investigated with one arrangement located upstream of the baseline separation location and the other two located downstream of the baseline separation. The slots were constructed by finding the intersection of a plane that originated at a constant x/R location. This plane was then rotated 23° about an axis formed by the intersection of the x/R station and $z/R = 0$ planes. The rotation angle was chosen so that

the slots would align with the separation location on the side of the fuselage as seen in Figure 8. The $x/R = 1.10$ set of slots were located just upstream of the flow separation location while the $x/R = 1.155$ and $x/R = 1.177$ are downstream. The intersection of the construction plane and the fuselage was broken into a set of eight slots with small gaps between each of the slots forming a near continuous U-shape. The eight slots resulted in a set of two slots on each side, two bottom slots, and two corner slots. Figures 8 and 9 shows the three sets of slot locations investigated in this study relative to the surface streamlines from the baseline simulation.

4.3.2 Jet Inclination Angle

The effect of the jet angle was numerically evaluated using OVERFLOW for the $x/R = 1.155$ slot location for steady blowing in free-air over a range of α_j from 15° to 90° with a slot height of 0.015" and a jet velocity ratio, U_j/U_∞ of 2.0. Figure 10 shows the fuselage drag to be fairly flat for α_j at 15° and 25°. At 30° the value of C_D jumps and continues to increase as α_j increases. Above $\alpha_j = 45°$ the drag is higher than the baseline C_D of 0.114 as the jets become less effective in attaching the flow on the ramp. From this comparison, a jet inclination angle of 15° and 25° performed best. Unless otherwise noted, an angle of 15° was used for further CFD simulations in this paper.

The steady blowing also generated thrust in the axial direction as shown in Figure 10. For the 0.015" slot height case and a velocity ratio of 2.0, the thrust contribution can be as high as 50% of the total baseline drag. This large contribution of thrust from the jets shows that a significant amount of blowing is being used and may not be practical for a real rotorcraft vehicle. However, insights gained from this study may help identify the flow mechanism for drag reduction resulting in a lower cost flow control approach.

4.3.3 elsA Jet Angle and Nominal Velocity Ratio

Both the U-shaped slot layout and the shape of the fuselage introduce some difficulties for the surface blowing boundary condition as implemented in elsA. As discussed in Section 3.2, only a single orientation angle can be specified for each slot. So, the jet angle is defined as the angle between the orientation angle and the average surface tangent vector down the slot. The indicated slot width is the width of the slot on the surface of the fuselage. Any change in curvature down the slot also introduces a non-uniform jet velocity down the slot. The exit velocity for each slot is set at the same location as the orientation angle so that the desired velocity ratio is achieved. This nominal velocity ratio is the value reported in the discussions that follow. If the slot has any curvature down its length, the velocity changes from this nominal value. For some of the slots this is not much of an issue, for example for slots 4 and 5, just upstream of the ramp, a nominal velocity ratio of 1.5 results in velocity ratios that range from 1.4 at one end of the slot to 1.6 at the other. For slot 7, along the side of the fuselage, the change in curvature down the slot causes significant problems. For this slot, a nominal velocity ratio of 1.5 results in a velocity ratio variation down the slot from 0.90 to 3.0.

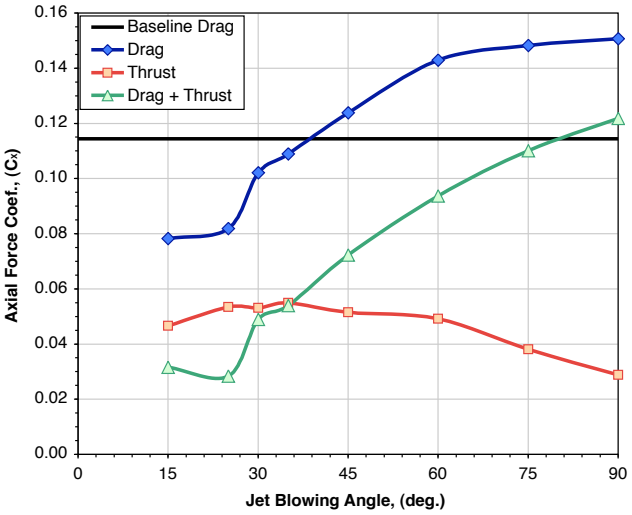

Figure 10: Evaluation of a jet angle, α_j, sweep for the slot at $x/R = 1.155$ for the free-air case with a slot width of 0.015" and a $U_j/U_\infty = 2.0$. Axial force coefficient for drag on the body and thrust generated by blowing slots. (OVERFLOW Results)

4.3.4 Steady Blowing

Steady blowing results were used as one way to evaluate the location and height of the slots. The CFD simulations were made using steady-state calculations requiring less computational resources as compared to time-accurate calculations needed for the unsteady flow control cases. The performance of the steady blowing was evaluated by looking at C_D as a function of C_μ and is presented in Figure 11. A jet inclination angle of $\alpha_j = 15°$ was used in this comparison. This figure also compares CFD results with and without the RCC to the turbulence model and LMP (from OVERFLOW). While using LMP greatly improved the steady-state convergence, utilizing the RCC has a larger effect on the drag results. Without experimental data to compare against for the steady blowing cases, it is unclear as to the validity of the RCC model for this type of flow simulation. All drag results reported for the steady blowing comparisons are computed from the viscous and pressure contributions acting on the fuselage, neglecting the thrust generated by the mass flux at the surface. It is also noted that the pressure force acting on the jet blowing boundary surface has not been included in the fuselage drag values given below.

Slot Location

The results presented in Figure 11 indicate, for the slot locations considered here, that the slot located at $x/R = 1.10$ is the poorest performing slot location. This slot location predicts a maximum drag reduction of 11% for the 0.015" slot at $C_\mu = 0.060$ without RCC. This slot

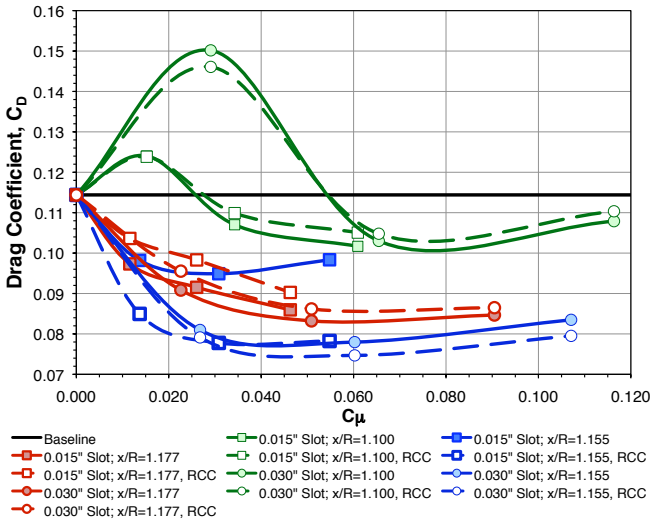

Figure 11: Summary of drag versus C_μ for steady blowing at three different slot locations and two slot widths with $\alpha_j = 15°$. CFD results with and without RCC and LMP are shown (OVERFLOW results).

location also shows a large drag increase for the lower blowing rates. The $x/R = 1.10$ slot location does attach the flow on the ramp for the low blowing case however it does not result in an increased base pressure on the ramp. The attached flow region just down stream from the slot produces a suction pressure resulting in a net drag increase for the low blowing case. Moving the slot downstream to $x/R = 1.155$ significantly improves the performance and the minimum drag, a drag reduction of 35% is achieved with 0.030" slots with RCC. This minimum drag point is at a $C_\mu = 0.060$, which corresponds to a $U_j/U_\infty = 1.5$. The smaller slot height of 0.015" at the $x/R = 1.155$ location also performs well for $C_\mu = 0.030$, which is half the jet momentum of the 0.030" slot. However, it is noticed that the performance of the 0.015" slot at $x/R = 1.155$ is very sensitive to the RCC. With RCC, this slot has a drag reduction of 32% and without RCC the drag reduction is only 17%. However, the other slot configurations have a much smaller sensitivity to the RCC term. Moving the slot even farther downstream to $x/R = 1.177$, results in a decrease in performance. Here a maximum drag reduction of 27% is achieved by the 0.030" wide slot without RCC. Based upon these results, the slot at $x/R = 1.155$ using RCC performed the best.

The results obtained with elsA are quite close to those from OVERFLOW. The $x/R = 1.155$ configuration also provides a significant drag reduction (up to 30% for the best configuration). The smaller slots perform comparably: the minimum drag point is obtained for $U_j/U_\infty = 1.5$. However the trend is different for the 0.030 slots: the higher the velocity, the lower the drag (for U_j/U_∞ varying between 1 and 2). This distinction from the OVERFLOW results may be explained by the jet boundary condition which is not identically defined between the two solvers. The turbulence models used (SA for OVERFLOW, k-ω Kok for elsA) may also have an effect on the results. These observations emphasize the sensitivity of drag values on numerical parameters.

Ramp Streamline and Surface Pressure

A rear view of the ramp region in Figure 12 shows the effect of the steady blowing on the surface pressure and streamlines for the $x/R = 1.155$ slot location and a slot height of 0.015". This figure shows the baseline flow (i.e., no blowing) for the free-air case which has a $C_D = 0.1144$. Increasing the blowing rate to $U_j/U_\infty = 1.0$ shows a significant increase of the base pressure on the ramp region with a decrease in surface pressure on the corners reducing the fuselage C_D to 0.0850. This velocity ratio moves the flow separation location inward, reducing the size of the separated region. Increasing the velocity ratio to 1.5 further increases the base pressure resulting in a reduction in C_D to 0.0778. The base pressure region is much higher for the 1.5 velocity ratio case however it is more concentrated. The $U_j/U_\infty = 2.0$ has an even higher base pressure region with the value of $C_D = 0.0782$, which is slightly higher compared to the 1.5 velocity ratio case. With increased blowing rates, the flow becomes more attached in the ramp region resulting in a base pressure increase and a corresponding reduction of the fuselage drag. Also with the increased velocity ratio, the value of C_P on the corners of the ramp region becomes increasingly negative contributing to an increase of the fuselage drag.

Separation and Velocity Vectors

A side view of the fuselage in Figure 13 helps to see the reduction of the size of the separated region, by plotting the velocity vectors and contours of the velocity deficit in the symmetry plane for the baseline and $U_j/U_\infty = 1.5$ cases at the $x/R = 1.155$ slot location and a slot height of 0.015". Regarding the separated region, results for the three velocity ratios were quite similar, hence the only the $U_j/U_\infty = 1.5$ case is presented in Figure 13. As it had already been stressed thanks to the baseline case, elsA results predict a lower overall fuselage drag as compared to OVERFLOW results but the $U_j/U_\infty = 1.5$ velocity ratio provides the maximum drag reduction in both cases. Steady blowing decreases the velocity deficit downstream from the ramp region and the flow remains attached much longer. The decreased Cp value on the corners of the ramp, already noticed in Figure 12, is also encountered in the symmetry plane at the beginning of the ramp.

Centerline Pressure

The effect of the steady blowing on the centerline and spanwise C_P values for the $x/R = 1.155$ slot are shown in Figures 14 and 15 for the OVERFLOW results. Figure 14 shows that increasing the jet velocity ratio increases the suction peak on the bottom of the ramp region near the flow separation as was seen by the low pressure regions in Figure 12. The centerline C_P values downstream of the ramp increase with higher values of U_j/U_∞. The C_P values on the upper surface of the fuselage are relatively unaffected by the steady blowing.

Spanwise Pressure

The spanwise OVERFLOW C_P results in Figure 15 are on the ramp along a constant z/R = -0.075 plane for the $x/R = 1.155$ slot location. This figure shows the baseline

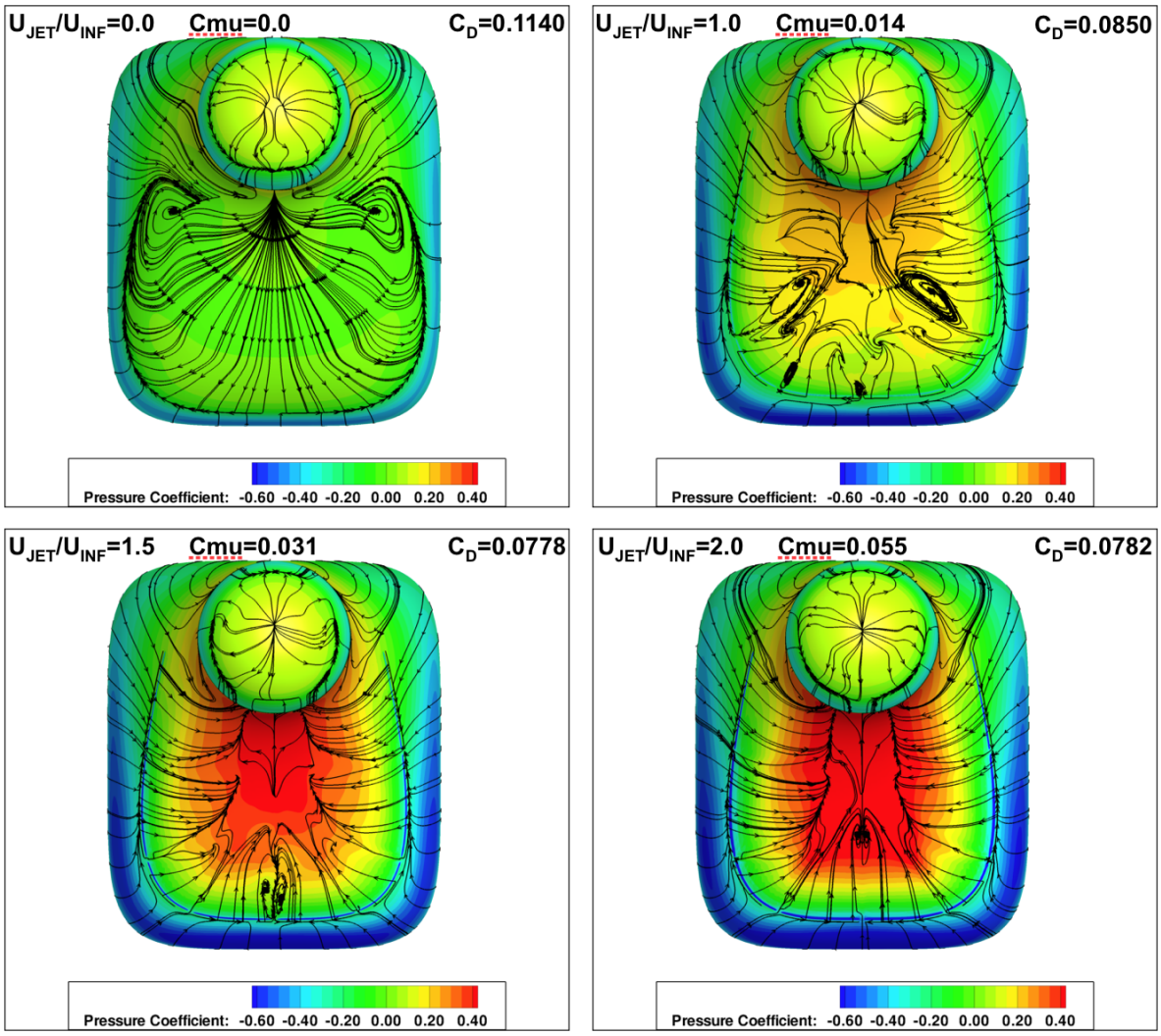

Figure 12: Rear view of ramp region of fuselage for the baseline flow and with steady blowing using slot configuration $x/R = 1.155$ and a slot width of 0.015" (OVERFLOW results).

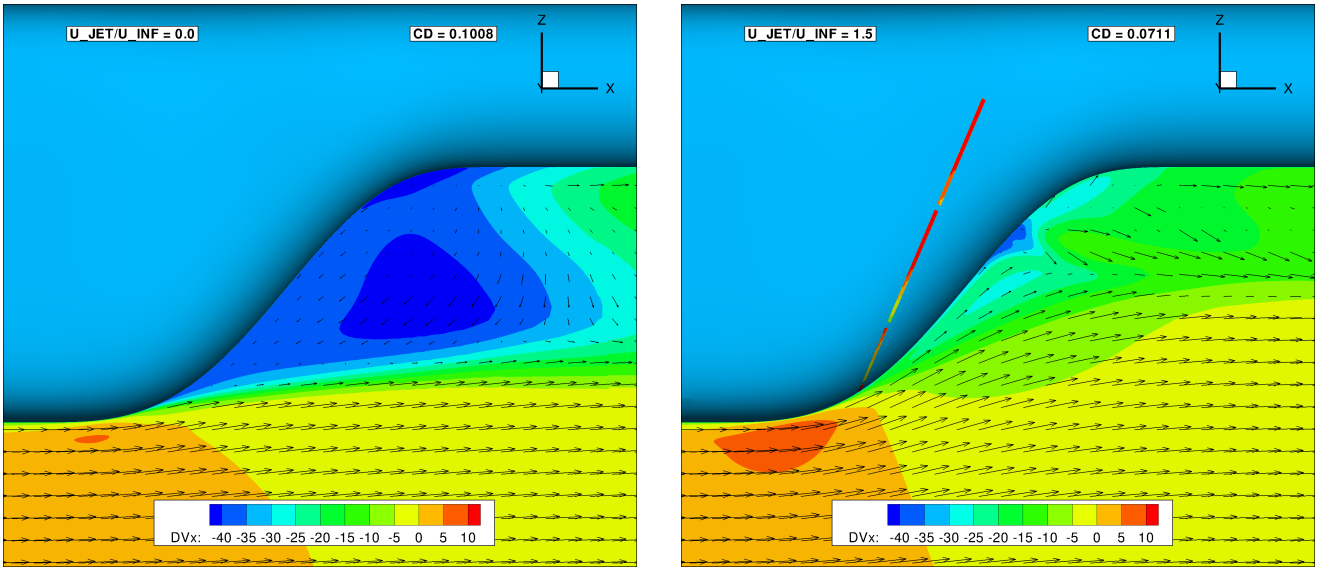

(a) $U_j/U_\infty = 0.00$, $C_D = 0.1008$

(b) $U_j/U_\infty = 1.50$, $C_D = 0.0711$

Figure 13: Side view of the fuselage for the baseline flow and with steady blowing for the slots at x/R=1.155 and a slot width of 0.015. DV_x is a velocity deficit, $DV_x = U_x - U_\infty$ (elsA results).

experimental data with the baseline CFD results with and without the tunnel walls and model support. Comparing the baseline experiment and CFD results show that the CFD is predicting the base pressure at the center of the ramp well however the peak suction pressure near separation is under predicted by the CFD by approximately 10%.

The steady blowing CFD results indicate an increasing base pressure on the center of the ramp for an increasing jet velocity ratio. This figure also shows the reduction of the pressure at the corners of the ramp region increasing the fuselage drag. Therefore a balance must exist for the steady blowing between increasing the base pressure at the center of the ramp without creating a large suction pressure at the corners. The spanwise C_P plots highlight why increasing the jet C_μ beyond a given point results in an increase of the fuselage drag.

4.3.5 Unsteady Zero-Net-Mass-Flux Blowing

Unsteady ZNMF jets were simulated in the CFD by modifying the surface boundary condition used for steady blowing by adding a sinusoidal fluctuation term defined as:

$$\rho_j U_j(t) = (\rho_j U_j)_\circ \sin(2\pi f t + \phi) \qquad (2)$$

where f is the frequency and ϕ the phase. Initially, the unsteady ZNMF CFD simulations were made with all eight blowing slots operating in phase with each other with a 0.015" slot at $x/R = 1.155$ and an $\alpha_j = 15°$ in free-air. The in-phase ZNMF jets OVERFLOW results are given in Figure 16. These results show a drag reduction, however there are large oscillations. Phasing the ZNMF jets such that each slot is 180° out of phase from its adjacent slot resulted in a significant reduction in these oscillations as well as a lower mean drag value. Similar trends have already been emphasized by Potsdam and Le Pape [22] when studying active flow control on a NACA0036: out-of-phase jets produced much lower oscillations in the computations and also reduced the model vibration in the wind tunnel section. The data presented in Figure 16 also indicates that the ZNMF blowing has a drag reduction of 26% as compared to 35% for steady blowing at the same velocity ratio.

ZNMF Jet Frequency

The effect of the frequency of the ZNMF flow control jets was investigated using the $x/L = 1.155$ slot location with the 0.015" slot height and an $\alpha_j = 15°$ with each slot 180° out of phase from the adjacent slots. The results from the OVERFLOW simulations are presented in Figure 17 and compared to the baseline and steady blowing cases for the same slot location and slot height. The low frequency of $F^+ = 0.16$ results in a reduction of the fuselage drag, however, it has large oscillations. Doubling the frequency to $F^+ = 0.33$ resulted in an improved drag reduction as well as a decrease of the oscillations in drag. Increasing the frequency to $F^+ = 0.66$ results in a further reduction of drag and amplitude of the oscillations. Doubling the frequency to $F^+ = 1.31$ does not change the mean drag or oscillation amplitude as compared to the $F^+ = 0.66$ case. Figure 17 also shows the

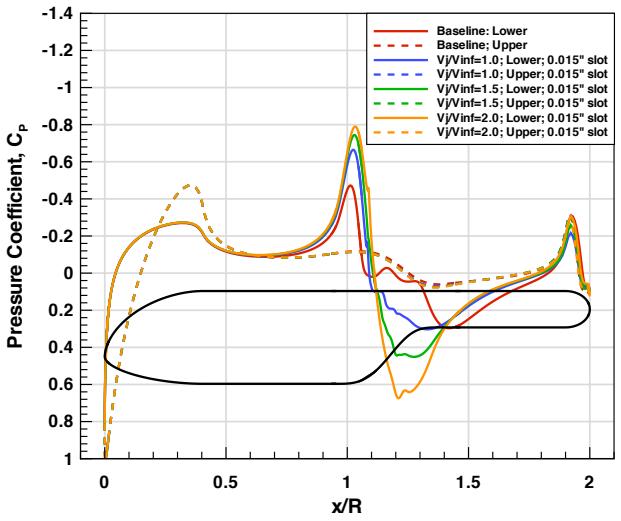

Figure 14: Centerline fuselage pressure for steady blowing (OVERFLOW results).

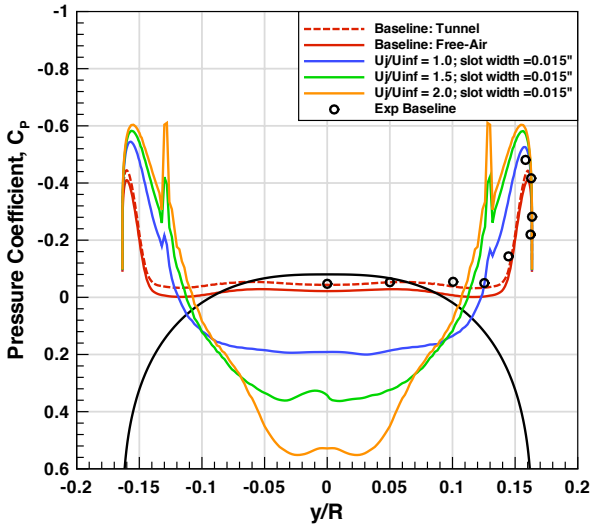

Figure 15: Spanwise surface pressure on ramp for the baseline case and steady blowing for the slot at $x/R = 1.155$ (OVERFLOW results).

$F^+ = 0.66$ ZNMF case to be approximately 10% higher than the steady blowing.

ZNMF Jet Velocity Amplitude

The influence of the ZNMF jet velocity amplitude was also examinated using the same slot location with the 0.030" slot height, $\alpha_j = 15°$, $F^+ = 1.0$, and each slot 180° out of phase from the adjacent slots. Those results are compared to the baseline case (elsA results) in Figure 18. Three synthetic jets nominal velocity ratios were investigated: VR= $U_j/U_\infty = 0.75$, 1, and 1.5. The low nominal velocity ratio, VR = 0.75, has smaller oscillations than the other two but also provides a lower drag reduction (-22%). Increasing the nominal velocity ratio to 1 results in a larger drag reduction of 27%, but with larger oscillations. The high nominal velocity ratio, VR = 1.5, has a drag reduction of 25%. The drag reduction obtained for the nominal VR = 1.0 and the nominal VR = 1.5 are very close. The trend seems to be similar to the one observed for steady blowing: increased

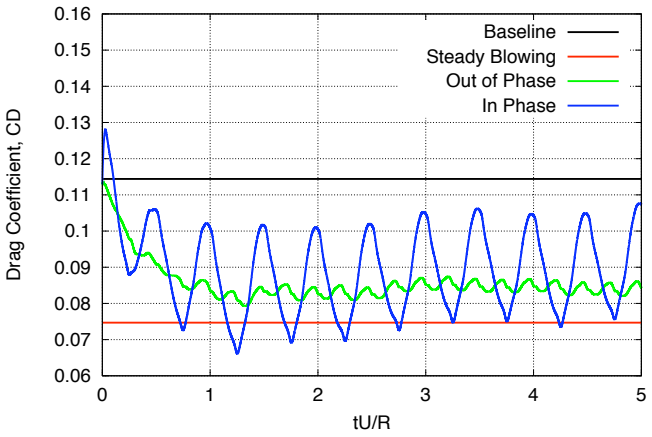

Figure 16: A comparison of in phase and out of phase using zero-net-mass-flux unsteady blowing for the slot at $x/R = 1.155$ in free-air. Slot width of 0.015" with $\alpha_j = 15°$ (OVERFLOW results).

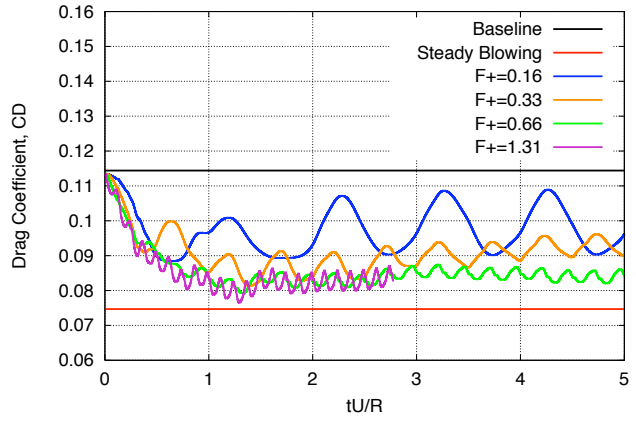

Figure 17: Effect of frequency on fuselage drag for unsteady zero-net-mass blowing for the slot at $x/R = 1.155$ in free-air. Slot width of 0.015" with $\alpha_j = 15°$ (OVERFLOW results).

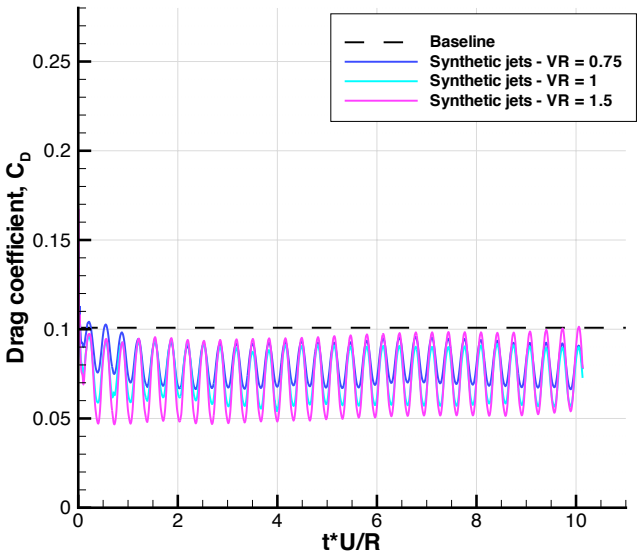

Figure 18: Effect of jet velocity ratio, U_j/U_∞, for ZNMF excitation at $x/R = 1.155$ (elsA Results).

blowing rates could reduce the fuselage drag but the increasingly negative pressure coefficient on the corners of the ramp region limits the gain.

ZNMF Jet Angle

The results presented in Figure 19 are used to complete the previous jet angle evaluation for steady blowing. The jet angle effect was evaluated for both 0.030" and 0.015" slots, a nominal jet velocity ratio U_j/U_∞ of 1.5 and $\alpha_j = 15°$, 30° and 45°. These simulations tend to confirm two previous conclusions drawn from steady blowing:

- The 0.030" and 0.015" slots, located at $x/R = 1.155$, perform quite comparably, even with ZNMF jets.
- A jet inclination angle of 15° provides better performance, the value of C_D increases when α_j exceeds 30°.

Phasing Configuration

The benefit of imposing a phase difference between adjacent slots has already been emphasized. Some additional simulations were then run to study the effect of the phasing on drag reduction. Four configurations from elsA computations are compared in Figure 20:

- $\phi = 0°$ for the eight slots (all eight slots working in phase).
- $\phi = 0°$ for slots 1,3,5 and 7, $\phi = 180°$ for slots 2, 4, 6 and 8 (adjacent slots out of phase).
- $\phi = 0°$ for slots 1, 4, 5, 8, $\phi = 180°$ for slots 2, 3, 6, 7.
- $\phi = 0°$ for slots 1, 2, 3, 4 and $\phi = 180°$ for slots 5, 6, 7, 8 (all slots on the right side in phase, as well as the slots on the left side, right and left sides out of phase).

Regarding only the drag coefficients, the phase difference both provides a slight lower mean drag value and a

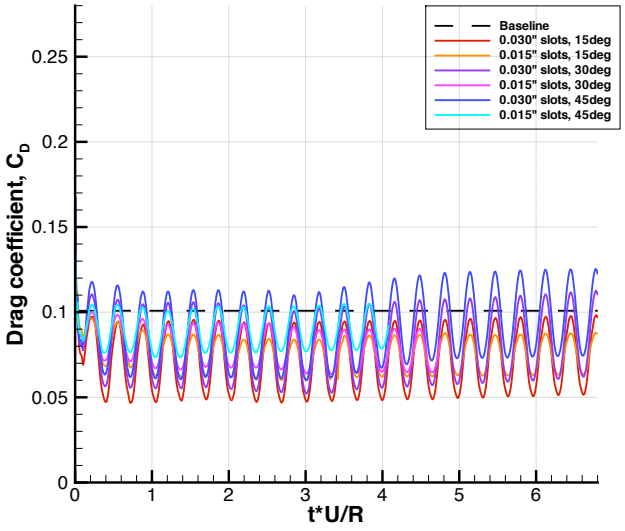

Figure 19: Effect of jet exit angle, α_j, for ZNMF excitation at $x/R = 1.155$ (elsA Results).

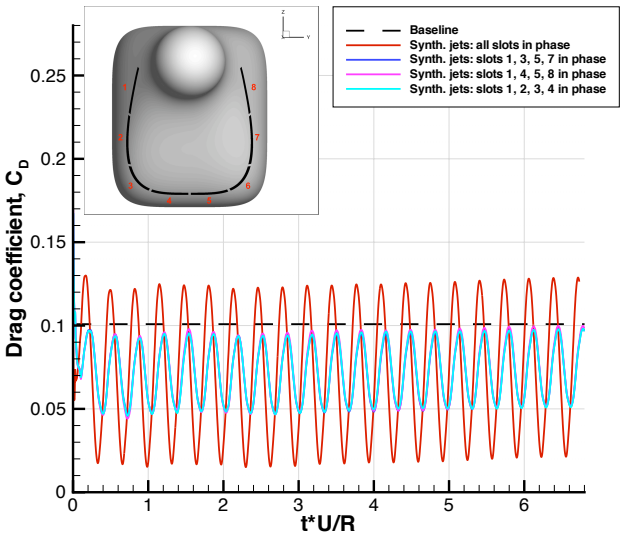

Figure 20: Effect of relative jet exit phasing, ϕ, for ZNMF excitation at $x/R = 1.155$ (elsA Results).

reduction of the oscillations but the phasing configuration does not seem to matter much: the drag is reduced by 25% for each case. A deeper study of the flowfield from each configuration is needed to better understand the flow mechanism of synthetic jets which leads to this drag reduction.

4.3.6 Effect of Angle of Attack on Flow Control

Simulations of the fuselage with flow control were made at two additional angles of attack to evaluate the sensitivity of the $x/L = 1.155$ slot location for a jet velocity ratio of $U_j/U_\infty = 1.5$. Figure 21 is a summary of CFD simulations made in free-air comparing the baseline to steady and unsteady ZNMF flow control. The baseline drag shows an increase in drag at both -5° and 5° angles of attack with the 5° case having a 15% increase in drag from the nominal 0° case. Steady blowing using the 0.030" height slot resulted in a fuselage drag reduction at -5°, 0°, and 5° with a near constant value of C_D for all angles. The smaller 0.015" slot performed similar to the 0.030" slot at -5°. Unsteady ZNMF blowing showed the 5° case to perform well improving the baseline drag at this angle of attack by 35% as compared to steady blowing at 40% for a slot height of 0.015". The unsteady blowing for the -5° case did not result in a drag reduction as compared to the baseline at the same angle of attack.

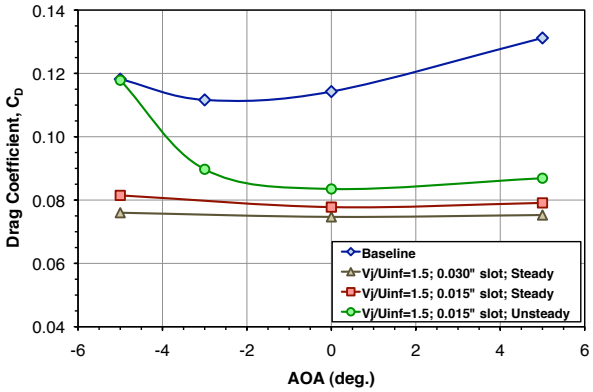

Figure 21: Sensitivity of the flow control for the slot at $x/R = 1.155$ for a constant $U_j/U_\infty = 1.5$ resulting in a $C_\mu = 0.030$. Simulations performed in free-air at a Mach number of 0.1 with $\alpha_j = 15°$ with OVERFLOW.

4.4 Flow Control Experiment

The experimental effort with actuation attempted to adapt the most effective ZNMF blowing drag reduction strategy from the computations to something that could be physically implemented into the model. The two side slots were merged into a single slot, as were the slots in the spanwise direction at the start of the ramp. This new three slot arrangement was implemented on a new tail and tailboom section. The spanwise slot is symmetric with respect to the centerline and 2.50 inches (63.50 mm) in length and 0.030 inches (0.762 mm) in width. The spanwise slot was oriented perpendicular to the local surface, with the downstream edge of the slot featuring a rounded edge that blended tangentially into the local surface. The other two slots are located on each side of the model and are each 2.40 inches (60.96 mm) in length and 0.015 inches (0.381 mm) in width. The side slots were oriented parallel to the y/R direction and each featured the same type of rounded downstream edge as the spanwise slot. The slots were located using the same 23° plane construction as the computations. The spanwise slot uses x/R= 1.110 as the starting point for the construction and the two side slots use x/R=1.15. The side slots share a common cavity that is driven 180° out of phase from the cavity for the spanwise slot. The two cavities are driven by the same active element, an electromechanical driven diaphragm, that is between the two cavities, naturally creating the 180° out of phase excitation for the cavities.

The performance of the actuation system was charac-

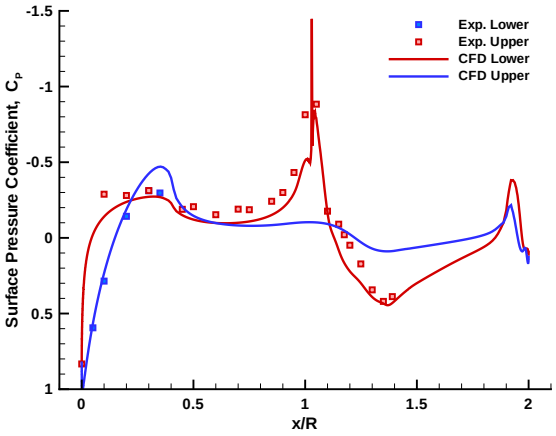

Figure 22: Comparison of the centerline surface C_P values from the experimental flow control case and the mean C_P values from the OVERFLOW simulation for 0° angle of attack and a free stream Mach number of 0.1

terized without the influence of an external flow. The cavities were designed with a goal of achieving a velocity ratio of 2, relative to the freestream velocity, out of each slot when the actuator was run at maximum power. This design goal was only realized for the spanwise slot. The maximum measured velocity for the spanwise slot was 68.5 m/s (VR = 1.98, F+ = 0.545), while for the side slots the maximum measured velocity was 54.2 m/s (VR = 1.57, F+ = 0.477). Since all the slots must operate at the same frequency, at the lower frequency, F+ = 0.477, the output of the spanwise slot was 65.8 m/s (VR = 1.91) resulting in a spanwise momentum coefficient of 0.0230 and a momentum coefficient for each side of 0.0075.

A comparison of the centerline surface pressure distribution from the experiment and the computation is presented in Figure 22. Even though the computation did not model the tunnel and model supports, there is a good agreement with the experimental centerline pressure data. For this case, the experiment saw a 15% increase in total drag and the computation saw a 25% increase. There is a lack of experimental data for the jet inclination angle that is required for the surface boundary condition. This probably leads to the CFD overpredicting the influence of the side slots and their effect on the drag.

5 Conclusions

Baseline CFD simulations agree well to the experimental data when modeling the tunnel and model support. Simulations run without the tunnel walls and model support will result in a lower computed drag. A comparison of the Cp profile on the model with and without walls and the model support shows a higher pressure on the nose and lower pressure on the ramp as a result of tunnel blockage by the model and support. This difference in the pressures on the model results in an increase fuselage drag for the simulation with the tunnel walls and model support. The drag coefficient for the 0° angle of attack case matches the experimental data and was under predicted by 3% for the -5° case. A comparison of the centerline C_P profiles shows good agreement between the CFD with tunnel walls and model support to the experimental data. Comparing the spanwise C_P data on the ramp shows a difference in the suction peak near separation for the 0° angle of attack case where the CFD under predicts this value. This difference is suspected to be a result of the simulations separating earlier than the experiment on the fuselage sides.

The location of blowing slots on the fuselage was evaluated using steady blowing where it was found that the slot at $x/R = 1.155$ had the best drag reduction performance. The inclination angle of the jet from the blowing slots was evaluated and jet angles of 15° and 25° were shown to perform the best for both steady and unsteady blowing. A comparison of the C_P plots for steady blowing indicates that the blowing acts to increase the base pressure on the center of the ramp. Analysis of the streamlines from the CFD simulations with flow control demonstrated that the extent of the flow separation region is reduced from the baseline uncontrolled case.

It was also found that phasing is a key element in ZNMF blowing flow control. An arrangement where each jet is 180° out-of-phase with its neighbor resulted in a lower mean drag with much smaller oscillations as compared to the case were the jets were all in-phase. Nevertheless, the choice of the phasing configuration did not seem to be of major importance with regards to drag reduction. Further thought needs to be given to synthetic jets flow mechanism to better understand the importance of phasing and the phenomenon resulting in drag reduction. CFD simulation over a range of frequencies and velocities showed that a $F^+ = 0.66$ and a $U_j/U_\infty = 1.5$ resulted in the best drag reduction performance. Evaluation of the flow control slot at $x/L = 1.155$ with $F^+ = 0.66$ at -5° and 5° angles of attack showed that steady blowing to perform very well both of these conditions. The unsteady ZNMF at the 5° angle of attack condition matched the steady blowing results, however, for the -5° case, the ZNMF blowing was not effective and did not improve the fuselage drag.

Acknowledgments

The NASA authors would like to thank Susan Gorton and the Subsonic Rotary Wing program for supporting and funding this research effort and its international cooperation. NWS would like to thank Jerome Harris for his assistance in conducting the PIV measurements and oil-flow visualizations.

Thomas Renaud and Jean-Christophe Boniface are also gratefully thanked by the ONERA authors for their contributions on the synthetic jet implementation and their help in resolving difficulties with the CFD simulations.

Appendix A - Fuselage Geometry Definition

The current research effort utilizes a modified version of the ROBIN (ROtor Body INteraction) fuselage. The underlying calculation procedure is outlined here for the convenience of the reader. For the values of the coefficients of the original ROBIN, the reader is referred to either Freeman and Mineck[5] or Mineck and Gorton [7].

The ROBIN fuselage shape is comprised of cross-sections that are defined analytically as a set of super-ellipses, the shape of which has been scaled to the rotor radius. The longitudinal coordinate, or station, x/R, down the length of the fuselage runs in an inclusive range from 0 to 2R, $0.0 \leq x/R \leq 2.0$. The coordinates that define the cross-sections, y/R and z/R, are derived from the polar coordinates that define the super-ellispe. The super-ellispe equations define the polar coordinate radius, r, as a function of 4 variables and 8 constants. One of those variables is the other polar coordinate, ϕ. The y/R and z/R cartesian coordinates are related to the polar coordinates r and ϕ by a standard coordinate transformation, with the exception that z/R is modified by an offset, Z_0.

The polar coordinate radius, r, is defined as follows:

$$r = \left[\frac{\left(\frac{H}{2}\frac{W}{2}\right)^N}{\left(\frac{H}{2}sin\phi\right)^N + \left(\frac{W}{2}cos\phi\right)^N} \right]^{1/N}$$

where $0 \leq \phi \leq 2\pi$ and $y/R = rsin\phi$ and $z/R = rcos\phi + Z_0$.

It is in the analytic definition of model height (H), width (W), camber (Z_0), and elliptical power (N), that the eight constants come into play and it is by changing these eight constants that different ROBIN shapes are possible. There is a different set of coefficients for each section of the ROBIN fuselage. Further control over the fuselage shape can be achieved by modifying the station location at which the change from one set of coefficients to another is made. The changes made to the coefficients give the ROBIN-mod7 fuselage its well-defined ramp region at the aft end of the fuselage, rectangular cross-section, and high tail boom. The constants are used in the definition of H, W, Z_0, and N as follows:

$$\begin{bmatrix} H(x/R) \\ W(x/R) \\ Z_0(x/R) \\ N(x/R) \end{bmatrix} = C_6 + C_7 \left(C_1 + C_2 \left(\frac{(x/R) + C_3}{C_4} \right)^{C_5} \right)^{1/C_8}$$

Once H, W, Z_0, and N are known, r can be calculated as a function of ϕ and the corresponding (r, ϕ) pairs can be transformed into the $(y/R, Z/R)$ coordinates for the cross-section at that station.

The coefficients used to generate the ROBIN-mod7 fuselage shape are presented in Table 5.

For 0.00 ≤ x/R < 0.40				
C_i	**H**	**W**	**Z_0**	**N**
C_1	1.0000	1.0000	1.0000	2.0000
C_2	-1.0000	-1.0000	-1.0000	3.0000
C_3	-0.4000	-0.4000	-0.4000	0.0000
C_4	0.4000	0.4000	0.4000	0.4000
C_5	1.8000	2.0000	1.8000	1.0000
C_6	0.0000	0.0000	-0.0800	0.0000
C_7	0.3825	0.3275	0.0800	1.0000
C_8	1.8000	2.0000	1.8000	1.0000
For 0.40 ≤ x/R < 0.96				
C_i	**H**	**W**	**Z_0**	**N**
C_1	0.3825	0.3275	0.0000	5.0000
C_2	0.0000	0.0000	0.0000	0.0000
C_3	0.0000	0.0000	0.0000	0.0000
C_4	1.0000	1.0000	1.0000	1.0000
C_5	0.0000	0.0000	0.0000	0.0000
C_6	0.0000	0.0000	0.0000	0.0000
C_7	1.0000	1.0000	1.0000	1.0000
C_8	1.0000	1.0000	1.0000	1.0000
For 0.96 ≤ x/R < 1.40				
C_i	**H**	**W**	**Z_0**	**N**
C_1	1.0000	1.0000	1.0000	1.0000
C_2	-1.0000	-1.0000	-1.0000	-1.0000
C_3	-0.9600	-0.9600	-0.9600	-0.9600
C_4	0.4400	0.4400	0.4400	0.4400
C_5	3.0000	3.0000	3.0000	1.0000
C_6	0.1500	0.1500	0.1163	2.0000
C_7	0.2325	0.1775	-0.1163	3.0000
C_8	0.1800	0.1800	0.1800	0.5500
For 1.40 ≤ x/R < 1.90				
C_i	**H**	**W**	**Z_0**	**N**
C_1	0.1500	0.1500	0.1163	2.0000
C_2	0.0000	0.0000	0.0000	0.0000
C_3	0.0000	0.0000	0.0000	0.0000
C_4	0.0000	0.0000	0.0000	0.0000
C_5	0.0000	0.0000	0.0000	0.0000
C_6	0.0000	0.0000	0.0000	0.0000
C_7	1.0000	1.0000	1.0000	1.0000
C_8	1.0000	1.0000	1.0000	1.0000
For 1.90 ≤ x/R ≤ 2.00				
C_i	**H**	**W**	**Z_0**	**N**
C_1	1.0000	1.0000	0.1163	2.0000
C_2	-1.0000	-1.0000	0.0000	0.0000
C_3	-1.9000	-1.9000	0.0000	0.0000
C_4	0.1000	0.1000	0.0000	0.0000
C_5	2.0000	2.0000	0.0000	0.0000
C_6	0.0000	0.0000	0.0000	0.0000
C_7	0.1500	0.1500	1.0000	1.0000
C_8	2.0000	2.0000	1.0000	1.0000

Table 5: Coefficients for the ROBIN-mod7 fuselage shape.

References

[1] Leishman, J. G., *Principles of Helicopter Aerodynamics*, Cambridge University Press, 2nd ed., 2006.

[2] Gatard, J., Costes, M., Kroll, N., Renzoni, P., Kokkalis, A., Rocchetto, A., Serr, C., Larrey, E., Filippone, A., and Wehr, D., "High Reynolds Number Helicopter Fuselage Test in the ONERA F1 Pressureized Wind Tunnel," 23rd European Rotorcraft Forum Paper 167, Dresden, Germany, September 16-18, 1997.

[3] Martin, P., Tung, C., Hassan, A., Cerchie, D., and Roth, J., "Active Flow Control Measurements and CFD on a Transport Helicopter Fuselage," American Helicopter Society 61st Annual Forum, Grapevine, TX, 2005.

[4] Ben-Hamou, E., Arad, E., and Seifert, A., "Generic Transport Aft-Body Drag Reduction using Active Flow Control," AIAA Paper 2004-2509, 2004.

[5] Freeman, C. and Mineck, R. E., "Fuselage Surface Pressure Measurments of a Helicopter Wind-Tunnel Model with a 3.15-meter Diameter Single Rotor," NASA TM 80051, Langley Research Center, March 1979.

[6] Phelps, A. E. and Berry, J. D., "Description of the U. S. Army Small-Scale 2-Meter Rotor Test System," NASA TM 87762 (AVSCOM TM-86-B-4), Langley Research Center, February 1987.

[7] Mineck, R. and Gorton, S. A., "Steady and Periodic Pressure Measurements on a Generic Helicopter Fuselage Model in the Presence of a Rotor," NASA TM 2000-210286, Langley Research Center, June 2000.

[8] Renaud, T., O'Brien, D., Smith, M., and Potsdam, M., "Evaluation of Isolated Fuselage and Rotor-Fuselage Interaction Using CFD," American Helicopter Society 60th Annual Forum, Baltimore, MD, June 2004.

[9] O'Brien, D. M. and Smith, M. J., "Analysis of Rotor-Fuselage Interactions Using Various Rotor Models," AIAA Paper 2005-0468, January 2005.

[10] King, R. A. and Breuer, K. S., "Acoustic Receptivity of a Blasius Boundary Layer with 2-D and Oblique Surface Waviness," AIAA Paper 2000-2538, 2000.

[11] Buning, P. G., Jespersen, D. C., Pulliam, T. H., Klopfer, W. M., Chan, W. M., Slotnick, J. P., Krist, S. E., and Renze, K. J., "OVERFLOW User's Manual Version 1.8m," Tech. rep., NASA Langley Research Center, 1999.

[12] Jespersen, D., Pulliam, T., and Buning, P., "Recent Enhancements to OVERFLOW," AIAA paper 97–0644, January 1997.

[13] Pulliam, T. H. and Chaussee, D. S., "A Diagonal Form of an Implicit Approximate-Factorization Algorithm," *Journal of Computational Physics*, Vol. 39, February 1981, pp. 347–363.

[14] Steger, J. L., Dougherty, F. C., and Benek, J. A., "A Chimera Grid Scheme," *Advances in Grid Generation*, edited by K. N. Ghia and U. Ghia, Vol. 5 of *FED*, ASME, New York, NY, 1983.

[15] Murphy, K., Buning, P., Pamadi, B., Scallion, W., and Jones, K., "Status of Stage Separation Tool Development for Next Generation Launch Technologies," AIAA Paper 2004-2595, June 2004.

[16] Spalart, P. and Allmaras, S. R., "One-Equation Turbulence Model for Aerodynamic Flows," AIAA Paper 1992-0439, 1992.

[17] Menter, R. F., "Two-Equation Eddy-Viscosity Turbulence Models for Engineering Applications," *AIAA Journal*, Vol. 32, No. 8, 1994, pp. 1598–1605.

[18] Shur, M., Strelets, M., Travin, A., and Spalart, P., "Turbulence Modeling in Rotating and Curved Channels: Assessing the Spalart-Shur Correction," *AIAA Journal*, Vol. 38, No. 5, May 2000, pp. 784–792.

[19] Cambier, L. and Veuillot, J. P., "Status of the elsA CFD Software for Flow Simulation and Multidisciplinary Applications," AIAA Paper 2008-664, January 2008.

[20] Barlow, J. B., Rae, W. H., and Pope, A., *Low-Speed Wind Tunnel Testing*, John Wiley & Sons, Inc., New York, 3rd ed., 1999.

[21] Loving, D. L. and Katzoff, S., "The Fluorescent-Oil Film Method and other Techniques for Boundary-Layer Flow Visualization," NASA TM 3-17-59L, Langley Research Center, March 1959.

[22] Potsdam, M. and Le Pape, A., "CFD Investigations on a NACA0036 Airfoil with Active Flow Control," AIAA Paper 2008-3869, 2008.